Morphological Changes in Block Copolymer Melts Due to a Variation of Intramolecular Branching. Dissipative Particles Dynamics Study

Jaroslav M. Ilnytskyi,* Taras Patsahan, and Myroslav Holovko

Institute for Condensed Matter Physics, National Academy, of Sciences of Ukraine, 1 Svientsitskii Str., 79011 Lviv, Ukraine

Peter E. Krouskop and Mike P. Makowski

PPG Industries, Coatings Innovation Center, 4325 Rosanna Drive, Allison Park, Pennsylvania 15101

Received May 8, 2008; Revised Manuscript Received August 26, 2008

ABSTRACT: We performed dissipative particles dynamics (DPD) simulations for the melts of various star and comb diblock copolymers with equal molecular weight ($L = 41$ beads) but with various types of internal branching. To assist formation of native morphologies, an anisotropic *NPT* ensemble was used. For the linear diblock polymer, we reevaluated the phase diagram in a high segregation regime and confirmed existence of the gyroid phase. The equilibrium morphologies and molecular conformations of branched molecules are compared with those found in the linear diblock copolymers at the same composition fraction. The analysis of the morphologies is performed in terms of metrics, spacial arrangement, and conformations of the molecules. Both weak (no phase change) and strong (phase changes) branching effects are observed. Promotion of a less ordered phase occurs in the case when highly constrained beads are unable to fill in required space regions (defined by the phase pitch) homogeneously. As a result, more ordered phase (observed for the linear diblock) cannot be formed. In some cases, an opposite effect is observed, e.g., promotion of more ordered lamellar phase (in place of the hexagonal one for the linear diblock) by suitable symmetry of the comb architecture.

1. Introduction

Block copolymers attracted much attention due to the recent increased interest in supramolecular chemistry.[1−3] The heart of the phenomena is the following mechanism. Two chemically different components of the polymer molecule tend to segregate, but macroscopic phase separation is prohibited by the intramolecular connectivity. As a result, microphase separation occurs, and a variety of phases can be formed depending on the fraction of each component, their chemical nature, and the type of intramolecular connectivity.[4−6] This made block copolymers good candidates for various applications.[7−9]

Focusing on the case of linear diblock copolymers, the phase diagram is examined in detail by the theoretical,[10−15] experimental,[5,16−18] and various simulational[19−25] techniques. The relatively new technique of dissipative particles dynamics (DPD) (see, for example, ref 26) was applied to linear diblock copolymer by Groot and Madden,[27] and we will remind some of their findings here. All the main phases predicted by mean field theory[13] have been reproduced. However, the authors pointed out some peculiarities, namely the existence of a perforated lamellar phase in place of the gyroid one and the shift of the phase diagram with respect to the theoretically predicted one.[13] The latter effect is explained by the finiteness of the chain length (10 monomers), which, in turn, lowers the effective value of the Flory−Huggins parameter χL (this will be discussed in more detail in section 2). Here and thereafter, we use L to denote the number of beads in one polymer molecule whereas N denotes the total number of beads in the melt.

More complex branched molecular architectures (e.g., comb, star, dendritic, and others) found much less coverage, and a smaller number of studies are available.[28−34] In particular, Turner et al.[28] performed experimental studies of the effect of chain topology on domain spacing in a heteroarm A_2B_2 star and in its linear counterpart AB. Domain spacings determined from TEM are ∼220 Å for the star polymer and much close value of 212 Å for the linear diblock (after the domain spacing is corrected with respect to its molecular weight).[28] Xu et al.[29] studied the phase diagram of two different star block copolymers: one with the homopolymer arms of A and B type and another with diblock-type arms of AB type. The phase diagram of the first architecture was found to be symmetric and much similar to that of the linear diblock copolymer but shifted toward larger values of χL. The phase diagram of the second architecture is asymmetric due to different topological constraints imposed on the core and tail components in this architecture. Also, the authors observed a range of transient (locally ordered) phases. Soto-Figueroa et al.[34] studied the molecular structures of poly(styrene)−poly(isoprene) copolymers with linear and 3-arm star architecture by DPD simulations. The mesoscopic parameters for the bead−bead interaction were obtained from styrene−isoprene molecular interaction. When the composition of the component homopolymer chains in each system was varied, the authors found ordered structures of body-centered-cubic, hexagonal packed cylinders, ordered bicontinuous double diamond, hexagonal perforated layers, and an alternating lamellar phase. Simulations agree well with the experimental findings.

It is quite evident that by introducing branching to diblock copolymer molecule, one imposes some restrictions on its conformational freedom. This, in turn, may influence the equilibrium morphology and its properties in each particular case. However, in our view, these effects are not well studied yet. The aim of our work is to perform a systematic analysis of this effect, using the DPD simulations. To this end, we considered a large set of architectures with the same molecular weight but with various type of internal branching. The set includes linear (nonbranched) molecules and various star and comb architectures. Each arm (or side chain) is always composed of beads of one sort, and the architectures are different in a number of A and B arms (side chains). The equilibrium

* Corresponding author. E-mail: iln@icmp.lviv.ua.

10.1021/ma801045z CCC: $40.75
Published on Web 11/21/2008

morphologies for all these branched architectures are obtained and analyzed, and their differences of that observed for linear molecules are discussed.

The outline of our paper is as follows: in section 2, we provide simulational details; in section 3, the reference phase diagram for the linear diblocks is discussed; in section 4, we study the properties of the phases; in sections 5 and 6, we present our primary results; and finally, our conclusions are given in section 7.

2. Simulations Details

All molecular architectures used in this study are of the same molecular weight defined in terms of a total number of beads in one molecule, $L = L_A + L_B = 41$ (here L_A and L_B are the number of beads for the component A and B, respectively). The total number of beads in a melt is $N = n_{mol}L$, where n_{mol} is a number of molecules.

We closely followed the DPD method as discussed by Groot and Warren.[35] Polymer molecules contain chain fragments linked in various ways; each fragment is of either sort A or B. The complete list of architectures is presented in the following sections. The adjacent beads are linked via harmonic bonds; the bonding force acting on the *i*th bead from its bond neighbor *j* is

$$\mathbf{F}_{ij}^{B} = -kr_{ij}\hat{\mathbf{r}}_{ij} \tag{1}$$

where $r_{ij} = |\mathbf{r}_{ij}|$, $\mathbf{r}_{ij} = \mathbf{r}_i - \mathbf{r}_j$, $\hat{\mathbf{r}}_{ij} = \mathbf{r}_{ij}/r_{ij}$, and $k = 4$ is the spring constant. Here and thereafter, the length, mass, time, and energy (k_BT^*) units are chosen to be equal to unity. Besides the bonding forces, each *i*th bead is subject to three nonbonded pairwise forces from its *j*th counterpart

$$\mathbf{F}_{ij} = \mathbf{F}_{ij}^{C} + \mathbf{F}_{ij}^{D} + \mathbf{F}_{ij}^{R} \tag{2}$$

namely, the conservative $\mathbf{F}_{ij}^{C}$, dissipative $\mathbf{F}_{ij}^{D}$, and random $\mathbf{F}_{ij}^{R}$ contributions

$$\mathbf{F}_{ij}^{C} = \begin{cases} a(1 - r_{ij})\hat{\mathbf{r}}_{ij}, & r_{ij} < 1 \\ 0, & r_{ij} \geq 1 \end{cases} \tag{3}$$

$$\mathbf{F}_{ij}^{D} = -\gamma w^{D}(r_{ij})(\hat{\mathbf{r}}_{ij}\cdot\mathbf{v}_{ij})\hat{\mathbf{r}}_{ij} \tag{4}$$

$$\mathbf{F}_{ij}^{R} = \sigma w^{R}(r_{ij})\theta_{ij}\Delta t^{-1/2}\hat{\mathbf{r}}_{ij} \tag{5}$$

Here $\mathbf{v}_{ij} = \mathbf{v}_i - \mathbf{v}_j$, $\mathbf{v}_i$ and $\mathbf{v}_j$ being the velocities of the beads, and θ_{ij} is Gaussian random variable: $\langle\theta_{ij}(t)\rangle = 0$, $\langle\theta_{ij}(t)\theta_{kl}(t')\rangle = (\delta_{ik}\delta_{il} + \delta_{il}\delta_{jk})\delta(t - t')$. One should mention that bonded pairs of beads (interacting via $\mathbf{F}_{ij}^{B}$ force) are not excluded from the repulsive nonbonded interaction $\mathbf{F}_{ij}^{C}$; hence, the equilibrium bond length is formed as a result of a compromise between these two forces. According to Español and Warren,[36] the dissipative and random force amplitudes are interrelated, $w^{D}(r_{ij}) = (w^{R}(r_{ij}))^2$ and $\sigma^2 = 2\gamma$, to satisfy the detailed balance. The frequently used analytical form is

$$w^{D}(r_{ij}) = (w^{R}(r_{ij}))^2 = \begin{cases} (1 - r_{ij})^2, & r_{ij} < 1 \\ 0, & r_{ij} \geq 1 \end{cases} \tag{6}$$

We used the value $\gamma = 6.75$. Parameter a in the conservative force $\mathbf{F}_{ij}^{C}$ defines maximum repulsion between two beads which occurs at complete overlap $r_{ij} = 0$. With two types of species, A and B, one has three repulsion parameters a_{AA}, a_{BB}, and a_{AB}, where one normally assumes $a_{AA} = a_{BB}$ and $a_{AB} > a_{AA}$ to promote components segregation. As was shown in ref 35, a_{AA} can be chosen to reproduce the correct compressibility of the DPD liquid, while $\Delta a = a_{AB} - a_{AA}$ can be related to the Flory−Huggins parameter χL[35]

$$\chi \sim 0.286\Delta a \tag{7}$$

at a number density equal to 3. By keeping L constant, all the simulations are performed at the same value of the Flory−Huggins parameter χL. To integrate the equations of motion, we used the modified velocity-Verlet algorithm by Groot and Warren.[35] It is known as a robust one, and we found it sufficiently accurate and efficient for the study of equilibrium morphologies. One, of course, can benefit from the development of newer algorithms discussed in ref 37.

In our preliminary simulations we have found that, with the use of constant volume ensemble, *NVT*, formation of some morphologies is much hindered. This happens when a typical pitch of the phase (e.g., lamellar width) is incommensurate with the dimensions of the box. To resolve this problem, the fragments of newly formed phase tend to rotate within the box until the optimal space arrangement for a new phase is found. As the result, the required simulation times increase dramatically. This situation is similar to the simulation of smectic liquid crystalline phases,[38] and the effect was also mentioned in the DPD simulations by Groot and Madden[27] and by Liu et al.[39] In view of this, we suggest using extended ensemble constant pressure $NP_{XX}P_{YY}P_{ZZ}T$ ensemble instead, which is implemented in the same way as in the molecular dynamics (MD) simulations (for more details on its implementation in MD, see ref 40). In brief, the box shape is kept cuboidal, but each dimension of it is free to change independently. These changes are governed by three separate Hoover barostats,[41] where the diagonal components of the pressure, P_{XX}, P_{YY}, and P_{ZZ}, are all set at required values. Normally, we choose a certain value for the total pressure, P^* (it can be estimated from a short *NVT* run at required density; this approach was also suggested in ref 42), and then set all three components equal, $P_{XX} = P_{YY} = P_{ZZ} = P^*/3$. In this way, instead of massive rearrangement of the polymer in the box, one observes self-adjustment of the box dimensions. In fact, this approach can be seen as a simplified variant of the Rahman−Parinello method.[44] In the latter, the more general, orthorhombic shape of the box is used.

As far as we are aware, the $NP_{XX}P_{YY}P_{ZZ}T$ ensemble has not been used in DPD simulations before, and a number of issues can be raised concerning its validity. As was shown by Jakobsen,[45] controlling pressure by the extended ensemble can lead to long-living high-frequency oscillations of the pressure if the simulations start far from equilibrium. This effect is quite similar to the temperature oscillations observed when using Nosé-Hoover thermostat[41] in MD simulations. Jakobsen has shown that the use of Langevin piston dampens these oscillations and provides much better equilibration of the pressure.[45] One should remark, however, that repulsion parameter a_{AA} in DPD simulations is interrelated to the density,[35] and therefore, any considerable compression (or extension) of the DPD melt without readjustment of a_{AA} could be seriously questioned. On the contrary, in the equilibrium, both the pressure and density fluctuations are small enough for this effect to be neglected. In the following section we test how $NP_{XX}P_{YY}P_{ZZ}T$ ensemble works in the case of a well-studied system of linear diblock copolymers and concentrate on the issues raised above.

We simulated the melts of $n_{mol} = 1000$. Following ref 35, the repulsion parameters $a_{AA} = a_{BB}$ are chosen to be equal to 25. One of supporting arguments for this choice is that at density $\rho^* = 3$ and $a_{AA} = a_{BB} = 25$ correct scaling for the polymer chain in athermal solvent was reproduced by the DPD simulations.[46] The a_{AB} parameter is 32; this corresponds to $\chi L \sim 82$, see ref 35). The time step of $\Delta t = 0.05$ is used. Typical pressure

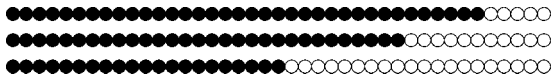

Figure 1. Linear diblock copolymer at various fraction of B component $f = L_B/L$ (A beads are shown in black, B beads in white).

is $P^* \sim 20$, box dimensions are $L_{XYZ} \sim 20-30$, and number of DPD steps are within the interval of $(2-8) \times 10^6$.

3. Linear Diblock Copolymer: Test for $NP_{XX}P_{YY}P_{ZZ}T$ Ensemble DPD Simulations and the Reference Phase Diagram

Linear diblock copolymers (Figure 1) are the most studied copolymers due to their simplicity. Self-consistent field theory predicts symmetrical phase diagram with the following sequence of phases: disordered (Dis), face-centered cubic (FCC), body-centered cubic (BCC), hexagonally arranged cylinders (Hex), gyroid (G), and lamellar (Lam) with the increase of one component fraction f from 0 to 0.5.[13] The G phase, however, was predicted to disappear at $\chi L > 60$. In the very recent study,[15] this phase diagram was reevaluated with the aim of describing better the strong segregation limit, indicating the presence of the G phase at least up to the value of $\chi L = 100$ in a narrow interval of $f \sim 0.31-0.35$.[15]

Groot and Madden performed comprehensive DPD simulations of a linear diblock copolymer phase diagram.[27] The chains were of the length $L = 10$, and most detailed simulations were performed at density $\rho^* = 3$, and for repulsion parameters $a_{AA} = a_{BB} = 25$ and $a_{AB} = 40$, this corresponds to the Flory−Huggins parameter of $\chi L \sim 46$.[27] As recalled by the authors, most of the simulations finally produce a phase structure predicted by the self-consistent field theory.[13] However, it was pointed out that the phase diagram obtained by the simulations at $\chi L \sim 46$ fits best with the theoretical phase diagram at a lower effective value of $\chi_{eff} L \sim 20$. The discrepancy was attributed to the finite length of the simulated chains, and a rough estimate for the relation between the two have been given:[27]

$$\chi_{eff} \approx \frac{\chi}{1 + 3.9L^{-0.51}} \tag{8}$$

Also, it was also mentioned that the perforated lamellar phase is found in place of the gyroid phase.[27] Authors suggest that the frustration of the periodicity of the gyroid phase and the box size is likely to force the system into the perforated lamellar phase, even if the gyroid phase is more favorable thermodynamically.[27] Similar remarks about the influence of finite size effects on phase formation were also made by Liu et al.[39]

The purpose of the reevaluation of the phase diagram for the linear diblock copolymers is twofold. First, we considered essentially longer molecules of $L = 41$ beads (as compared to ref 27) which allows us to construct a variety of branched diblock architectures with the same number of beads (considered in the following sections). In this way the phase diagram of linear diblocks will serve us as a reference one. Second, the $NP_{XX}P_{YY}P_{ZZ}T$ ensemble was employed, which has not been applied to the DPD simulations before. Therefore, the linear diblock case can be seen as an effective test on both accuracy of the simulations and reproducibility of the known phase diagram.

With the increase of the diblock length up to $L = 41$, the largest relaxation time τ grows significantly, $\tau \sim L^2$ (according to the Rouse theory). As the result, the microphase separation and formation of equilibrium morphologies are found to be rather slow at moderate values of $\chi L \sim 45$ ($a_{AA} = a_{BB} = 25$ and $a_{AB} = 28.9$), especially at some compositions for the diblocks. Because of this effect, we choose to use a higher value

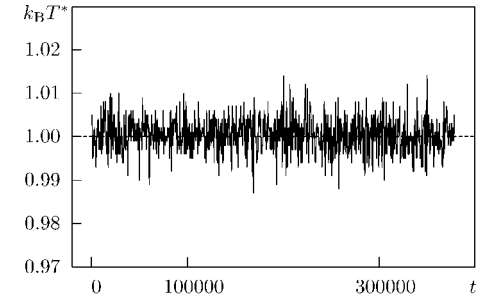

Figure 2. Reduced temperature k_BT^* vs time t (in DPD time units) for $NP_{XX}P_{YY}P_{ZZ}T$ extended ensemble DPD simulations of the linear diblock copolymer with $f = 0.244$.

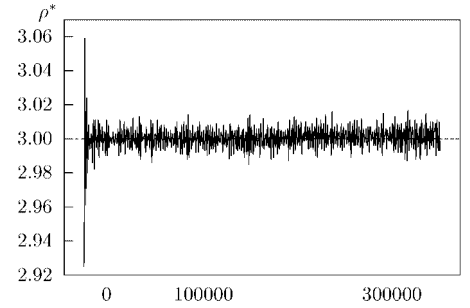

Figure 3. Reduced density ρ^* vs time t (in DPD time units) for $NP_{XX}P_{YY}P_{ZZ}T$ extended ensemble DPD simulations of the linear diblock copolymer with $f = 0.244$.

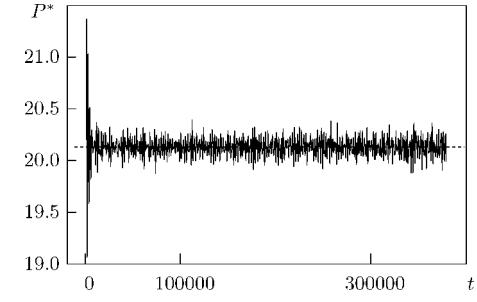

Figure 4. Reduced pressure P^* vs time t (in DPD time units) for $NP_{XX}P_{YY}P_{ZZ}T$ extended ensemble DPD simulations of the linear diblock copolymer with $f = 0.244$.

of $\chi L \sim 82$ ($a_{AA} = a_{BB} = 25$ and $a_{AB} = 32$). The following set of B component fraction was used: $f = 0.098$, 0.146, 0.195, 0.244, 0.293, 0.341, 0.390, and 0.488. The reduced total pressure P^* was chosen from the requirement that the average number density should be equal to $\rho^* = 3$.

To check the accuracy of the integration scheme, we monitored the fluctuations of the temperature, density, and pressure; these are shown in Figures 2−4 (the case of $f = 0.244$ is shown). At the very beginning, quick oscillations are observed for the density and pressure (maximum deviations from the average values are 2.3% and 4.4%, respectively). These oscillations quickly fade away, and in the equilibrium maximum deviations of the temperature, density, and pressure do not exceed 1.5%, 0.7%, and 1.3%, respectively. No systematic drift of these properties is observed.

In our reevaluation of the phase diagram of linear diblock copolymers of $L = 41$ beads in $NP_{XX}P_{YY}P_{ZZ}T$ ensemble, the following phases were identified: Dis ($f = 0.098$), FCC ($f = 0.146$), Hex ($f = 0.195$, 0.244, and 0.293), G ($f = 0.341$), and Lam ($f = 0.390$ and $f = 0.488$). The simulation times spawn up to 400 000 DPD units, i.e., 8×10^6 DPD steps. We have observed a number of intermediate phases (random pipe network, perforated lamellar phase, etc.) at $f = 0.195$, 0.244,

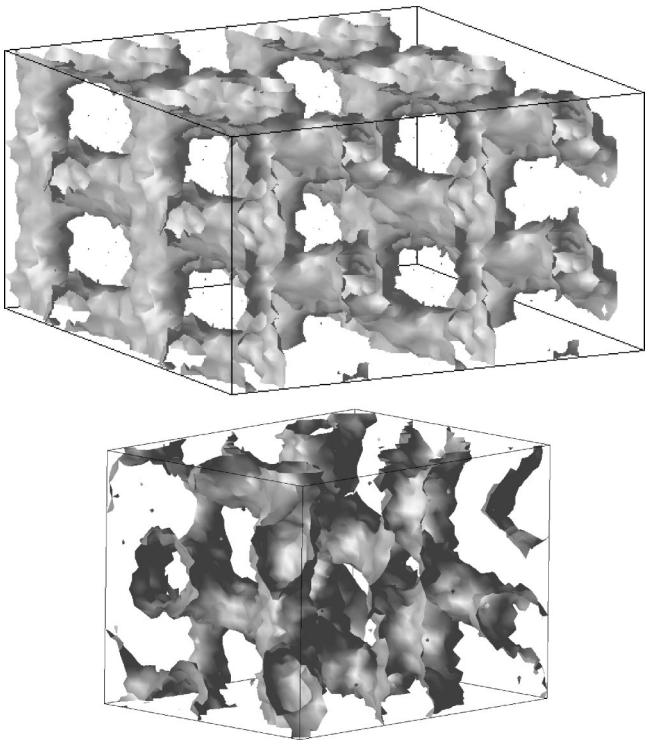

Figure 5. Density snapshots of gyroid phase (G) obtained at $f = 0.341$ for linear diblock copolymer. Top picture shows simulation box with 1000 molecules (replicated in space), and bottom picture shows larger box with 4000 molecules.

and 0.293. However, at the end of the simulation, these phases was shown to be metastable and disappear in favor of the hexagonal phase.

The density-coded snapshots for all phases are similar to those published before (e.g., ref 27); hence, we do not present these here. We would like to stress that at $f = 0.341$ we identified the gyroid phase and not the perforated lamellar phase as in ref 27; this could be attributed to the use of the $NP_{XX}P_{YY}P_{ZZ}T$ ensemble. For better visualization of this phase, the box was replicated in space and is shown in this form in Figure 5, top picture. To make sure that this phase is not an artifact of a periodic boundary conditions, we performed additional simulation of a larger system of $n_{mol} = 4000$ molecules. The snapshot indicates the same phase and is shown in Figure 5 (bottom).

The phases are marked as color coded circles in Figure 6, where we attempted to map these onto the phase diagram by Cochran et al.[15] at $\chi L \sim 82$ (top row of colored circles). Similarly to Groot and Madden,[27] we observed that the phase diagram obtained by DPD simulations maps the best onto the theoretical one if a lower effective value $\chi_{eff}L$ is used for the latter. We found this to be true in our case, and the estimated value is $\chi_{eff}L \sim 44$ (see Figure 6, lower row of colored circles). According to the approximate formula (8), this value should be around 52, but given the steepness of the slope for phase boundaries, we would comment that both values are reasonably close.

4. Properties of the Phases

To examine the effect of microphase segregation, a number of properties are evaluated and compared across different macrophases. First of all, we looked at the distribution of bond lengths throughout the melt, $f(l)$. These were averaged over all the molecules and along the time trajectory and are found to be the same in all phases (see Figure 7). Two distinct average curves, for the bonds between the same beads (marked via l_{AA}, l_{BB}) and the one between the different beads (l_{AB}), appear for

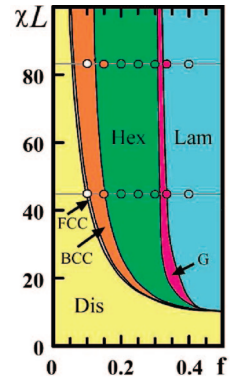

Figure 6. Mapping of phases identified in our DPD simulations at $\chi L \sim 82$ (shown as colored circles) onto the mean field phase diagram by Cochran et al.[15] Mapping is found to be poor if attempted at $\chi L \sim 82$ (upper row of colored circles) but is very good when done at effective value $\chi_{eff}L \sim 44$ (lower row). For $\chi_{eff}L$ see eq 8 (abbreviations of the phases follow these in the text.)

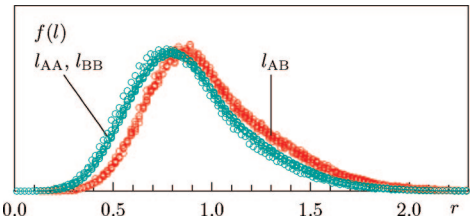

Figure 7. Bond length distribution. l_{AA} and l_{BB} mark bonds between similar beads and l_{AB} those between dissimilar beads; the curves in all phases are found to overlap.

obvious reason for stronger repulsion in latter case. One can conclude that no bond deformations are observed in any particular phase being examined. It is obvious that the width of this distribution depends on the choice of both repulsion parameters, a_{AA} and a_{AB}, and the stiffness of the harmonic bond force, k, and can be made narrower by appropriate choice of these parameters, if desired.[47] We choose the typical values (especially that for $a_{AA} = a_{BB}$) that are also used in a number of studies.[27,39,48,29,49] In our opinion, as far as the DPD beads do not represent atoms, but are rather imaginary agglomerates of these, the bond between two such objects has much broader physical meaning than that for the atomic system. The softness of the DPD interactions raises also the issue of chains crossability;[42,43] however, the latter is not expected to have any important effect on the equilibrium properties of the system but rather on its dynamics only.

The level of intramolecular segregation was examined in the following way. For each molecule, the centers of mass (COM) for each subchain (of component A and component B) were found, and the distance between these, R_{AB}, was evaluated (see Figure 8). Then the histogram for the R_{AB} distribution, $f(R_{AB})$, was built throughout the melt, and it was further averaged along the time trajectory. One can observe rather small drift of the $f(R_{AB})$ distribution at larger values of $f = 0.2-0.5$ (Hex−G−Lam sequence). On the contrary, the position of the $f(R_{AB})$ distribution changes remarkably at smaller values of f (Dis−FCC−Hex sequence, see Figure 9). One can suggest that the change in intramolecular segregation is important at Dis−FCC and FCC−Hex transitions only. We will plot the average values for R_{AB} against other properties below.

The changes in intramolecular segregation are also expected to affect the general shape of the molecules. This can be represented by the gyration tensor $\mathbf{G}^{[k]}$ defined for the kth molecule as

$$G_{\alpha\beta}^{[k]} = \frac{1}{N}\sum_{i=1}^{N}(r_{i,\alpha}^{[k]} - R_{\alpha}^{[k]})(r_{i,\beta}^{[k]} - R_{\beta}^{[k]}) \quad (9)$$

Here α, β denote Cartesian axes, $r_{i,\beta}^{[k]}$ are the positions of individual beads, and $\mathbf{R}^{[k]}$ is the position of the COM of the kth molecule. The eigenvalues of $\mathbf{G}^{[k]}$ are $(\sigma_{\alpha}^{[k]})^2$, where $\sigma_{\alpha}^{[k]}$ are the semiaxes of the equivalent ellipsoid for the kth molecule. The principal axes for this ellipsoid are defined by appropriate eigenvectors of $\mathbf{G}^{[k]}$. The trace of the gyration tensor defines squared radius of gyration of the molecule $(R_g^{[k]})^2$

$$\mathrm{Tr}\,\mathbf{G}^{[k]} = \sum_{\alpha=1}^{3}(\sigma_{\alpha}^{[k]})^2 = (R_g^{[k]})^2 \quad (10)$$

The latter can be averaged over all the molecules and also along a time trajectory (denoted below via indices k and t, respectively) and square rooted to provide the estimate for the average radius of gyration, R_g

$$R_g = \sqrt{\langle (R_g^{[k]})^2 \rangle_{k,t}} \quad (11)$$

The average hydrodynamic radius R_h can also be defined as

$$R_h^{-1} = \left\langle \frac{1}{N^2}\sum_{i\neq j}\frac{1}{r_{ij}^{[k]}} \right\rangle_{k,t} \quad (12)$$

where r_{ij} is the distance between the ith and jth bead within the kth molecule. The average semiaxes of molecular equivalent ellipsoids can be found in a similar way

$$\sigma_{\alpha} = \sqrt{\langle (\sigma_{\alpha}^{[k]})^2 \rangle_{k,t}} \quad (13)$$

We employed the following ordering: $\sigma_1 > \sigma_2 > \sigma_3$.

The numerical values for the averages R_{AB}, R_g, and σ_{α} are shown in Table 1. There we list also the square rooted component of the gyration tensor along the R_{AB} vector, T_{AB}. It should be equal to σ_1 in case when R_{AB} coincides with the long axis of the equivalent ellipsoid, or $T_{AB} < \sigma_1$ otherwise. In this way one can monitor whether or not the intramolecular segregation occurs along the principal axis of the molecule.

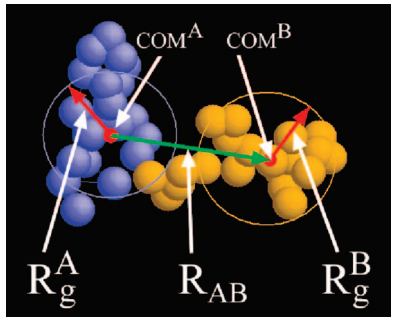

Figure 8. Illustration of splitting a molecule into A and B subsytems, showing partial COMs and radii of gyration and COM−COM separation vector R_{AB}.

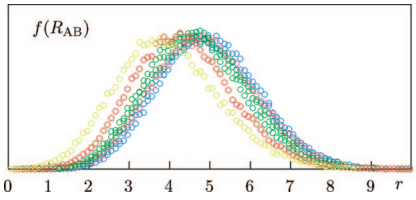

Figure 9. Distribution of COM−COM separation vector length R_{AB} in various phases (data are color-coded similarly to the phase diagram shown in Figure 6).

Table 1. Properties That Characterize Microphase Segregation in Linear Diblock Copolymer Melt at Different Values of B Component Fraction f[a]

f	R_{AB}	R_g	σ_1	σ_2	σ_3	T_{AB}	phase
0.000		2.655	2.324	1.098	0.665		uni
0.098	3.970	2.697	2.355	1.129	0.674	2.197	Dis
0.146	4.348	2.793	2.448	1.160	0.678	2.347	BCC
0.195	4.598	2.896	2.566	1.164	0.672	2.513	Hex
0.244	4.715	2.971	2.652	1.162	0.667	2.626	Hex
0.293	4.812	3.040	2.736	1.148	0.661	2.730	Hex
0.341	4.869	3.093	2.805	1.125	0.657	2.812	G
0.390	5.011	3.178	2.904	1.111	0.656	2.921	Lam
0.488	4.907	3.145	2.872	1.101	0.655	2.895	Lam

[a] R_{AB} is the COM−COM separation vector length, R_g is molecular radius of gyration, $\sigma_1 > \sigma_2 > \sigma_3$ are the semiaxes of equivalent molecular ellipsoid, and T_{AB} is the component of the tensor of gyration along $\mathbf{R}_{AB}$. Uniform phase at $f = 0.0$ is abbreviated as "uni"; other abbreviation follow those at the beginning of section 3.

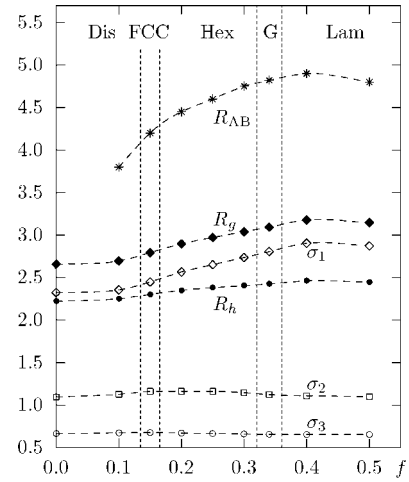

Figure 10. Effect of the increase of microphase separation on various properties of linear diblock copolymer melt (see text for notations).

The average values R_g, R_h, σ_{α}, and R_{AB} are also plotted in Figure 10. One can see that with the introduction of a relatively small fraction of B component ($f = 0-0.2$) the intramolecular phase segregation becomes apparent as a rapid increase of R_{AB} is observed (see Figure 10). This, in turn, promotes elongation of the molecular coil (monitored by σ_1) and both radii, R_g and R_h, increase. With the further increase of B component fraction, $f = 0.2-0.5$, however, this effect slows down and eventually saturates (see Figure 10). One can conclude that the increase of intramolecular segregation is playing a part in the Dis−FCC and FCC−Hex transitions only. On the contrary, the G−Hex and Hex−Lam transitions occur at almost constant level of internal segregation (and at constant molecular shape); hence, molecular rearrangement could be seen as the only mechanism behind these transitions.

As far as the microphase separation occurs in every phase, the melt is always split into the type A and type B submelts. Each submelt contains molecular subchains of the length $L_A = (1 - f)L$ and $L_B = fL$, respectively, and one can raise the question of the properties of these submelts, for instance, the scaling laws for the subchains radii of gyration. To this end, we consider the partial radii of gyration R_g^A and R_g^B defined similarly to eqs 9−11, but for each respective subchain only (see Figure 8). Similarly to the case of whole molecule, one can find an equivalent ellipsoid for each component and evaluate its semiaxes. The average values for the principal semiaxes of each component, σ_1^A and σ_1^B, along with the R_g^A, R_g^B, and square

Table 2. Properties of A and B Subsystems in Linear Diblock Copolymer Melt at Different Values of B Component Fraction *f*[a]

f	R_g^A	R_g^B	σ_1^A	σ_1^B	T_A	T_B	phase
0.000	2.655	0.000	2.324	0.000			uni
0.098	2.510	0.713	2.193	0.642	1.869	0.431	Dis
0.146	2.448	0.935	2.140	0.829	1.800	0.597	BCC
0.195	2.389	1.109	2.091	0.978	1.764	0.727	Hex
0.244	2.316	1.268	2.029	1.118	1.694	0.855	Hex
0.293	2.240	1.407	1.964	1.241	1.632	0.969	Hex
0.341	2.170	1.514	1.906	1.330	1.590	1.041	G
0.390	2.119	1.619	1.867	1.419	1.575	1.107	Lam
0.488	1.891	1.841	1.660	1.617	1.349	1.309	Lam

[a] $R_g^{A,B}$ is partial radius of gyration, $\sigma_1^{A,B}$ is main semiaxis of partial equivalent ellipsoid, and $T_{A,B}$ is the component of gyration tensor along $\mathbf{R}_{AB}$; A and B denote the A and B subsystems, respectively.

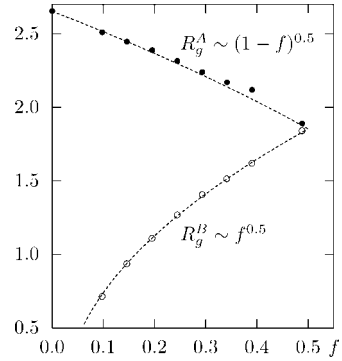

Figure 11. Scaling laws for the submelts A (solid circles) and B (hollow circles) in linear diblock copolymer melt studied via the partial radii of gyration.

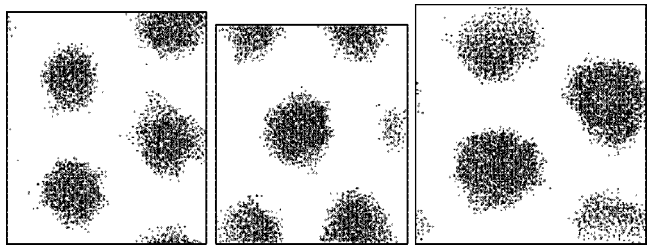

Figure 12. In-scale comparison of the Hex phase pitch in linear diblock copolymer melt at $f = 0.195$, 0.244, and 0.293 (from left to right); the centers of B beads are shown as black dots.

rooted components of the gyration tensor along the R_{AB}, namely, T_A and T_B, are listed in Table 2.

Scaling properties for R_g^A and R_g^B are examined in Figure 11, and it is evident that both radii obey the same scaling law (with the appropriate subchain length, L_A and L_B, respectively). The exponent $\nu = 0.5$ is the same as for the one-component melt.[50] This indicates that the scaling properties of submelts (at least as seen by the R_g behavior) are not affected by the particular phase and reproduce those for the one-component melt.

The Hex phase is the broadest one in *f*, and it is interesting to compare its pitch in all three cases, $f = 0.195$, 0.244, and 0.293. The cross sections of the snapshots performed perpendicularly to cylinders of the B component are presented in Figure 12 (the centers of B beads are marked by black dots; A beads are not shown). We found that the hexagonal spacing is almost the same in all three cases, and the main difference is in the thickness of the cylinders, obviously due to the change of the components fraction. One should remark that for the existence of the Hex phase the length of the A component subchains should be sufficient to fill in the gaps between the cylinders. We will return to this issue below.

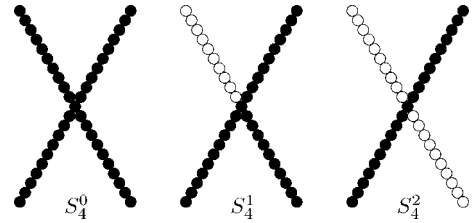

Figure 13. Star architectures with 4 arms (A beads are shown in black, B beads in white).

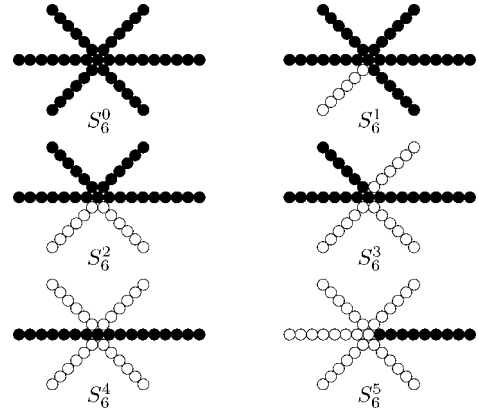

Figure 14. Star architectures with 6 arms (A beads are shown in black, B beads in white).

5. Star Diblocks

The following notation is introduced for the stars architectures being considered in this study. S_β^q is the star with total number of *p* arms and *q* of them are of type B. We consider 4- and 6-arm stars; all the architectures are shown in Figures 13 and 14. As was pointed out above, all architectures has the same number of beads, $L = 41$, where $L_A = (1 - f)L$ of them are of sort A and $L_B = 41f$ of sort B.

We should note that our set of star diblock copolymers differ essentially from that considered recently by Xu et al.[29] In that study only symmetric cases were considered, A_nB_n and $(AB)_n$, where the former type can be represented as S_{2n}^n in our notations, whereas in the latter one, each arm of the star is a linear diblock by itself.

Before discussing the morphologies of star diblock copolymers, let us make some general comments first. The equilibrium morphology can be seen as a compromise among three of the following requirements: (1) uniform density throughout the box (due to the presence of repulsive forces between all the pairs of beads); (2) minimum interface area which separates beads of a different sort (due to stronger repulsion between different beads); and (3) imposed constraints on the conformations (due to the intramolecular connectivity).

Each star architecture considered in our study can be compared to the appropriate linear diblock with the same components fraction *f*. In the case of weak branching effect, the same phase is expected as for the linear counterpart, while for the strong branching effect, the phase is expected to change.

We calculated the same set of properties as for the linear diblock case (see Tables 3 and 4). There is also one additional column, "ref", which indicates the reference phase that takes place for the linear $L = 41$ diblock at the same value of *f*. In most cases weak branching effect was observed, and the phases coincide with the "ref" phases. In the case of S_4^1, S_6^4, and S_6^5 stars, the strong branching effect is observed, where the phases are shifted toward the ones observed at smaller *f* for linear diblocks.

Table 3. Properties That Characterize Microphase Segregation in Star Diblock Copolymer Melt at Different Values of B Component Fraction f[a]

	f	R_{AB}	R_g	σ_1	σ_2	σ_3	T_{AB}	phase	ref
S_4^0	0.000		2.146	1.708	1.101	0.690		uni	uni
S_4^1	0.244	3.046	2.285	1.817	1.189	0.712	1.703	**FCC**	**Hex**
S_4^2	0.488	3.124	2.361	1.927	1.174	0.694	1.894	Lam	Lam
S_6^0	0.000		1.873	1.423	1.004	0.691		uni	uni
S_6^1	0.146	2.228	1.910	1.444	1.029	0.709	1.251	FCC	FCC
S_6^2	0.293	2.356	1.959	1.493	1.056	0.703	1.402	Hex	Hex
S_6^3	0.439	2.422	1.984	1.534	1.049	0.695	1.492	Lam	Lam
S_6^4	0.585	2.430	1.995	1.552	1.042	0.697	1.514	**G**	**Lam**
S_6^5	0.780	2.649	1.972	1.517	1.044	0.704	1.456	**FCC**	**Hex**

[a] The notations follow those in Table 1.

Table 4. Properties of A and B Subsystems in Star Diblock Copolymer Melt at Different Values of B Component Fraction f[a]

	f	R_g^A	R_g^B	σ_1^A	σ_1^B	T_A	T_B	phase	ref
S_4^0	0.000	2.146	0.000	1.708	0.000			uni	uni
S_4^1	0.244	2.003	1.236	1.659	1.086	1.034	0.917	**FCC**	**Hex**
S_4^2	0.488	1.743	1.744	1.479	1.489	0.999	0.969	Lam	Lam
S_6^0	0.000	1.873	0.000	1.423	0.000			uni	uni
S_6^1	0.146	1.832	0.900	1.435	0.795	0.969	0.651	FCC	FCC
S_6^2	0.293	1.751	1.275	1.406	1.080	0.889	0.747	Hex	Hex
S_6^3	0.439	1.627	1.481	1.325	1.219	0.885	0.746	Lam	Lam
S_6^4	0.585	1.504	1.628	1.262	1.309	0.939	0.805	**G**	**Lam**
S_6^5	0.780	1.147	1.726	1.006	1.342	0.860	0.900	**FCC**	**Hex**

[a] The notations follow those in Table 2.

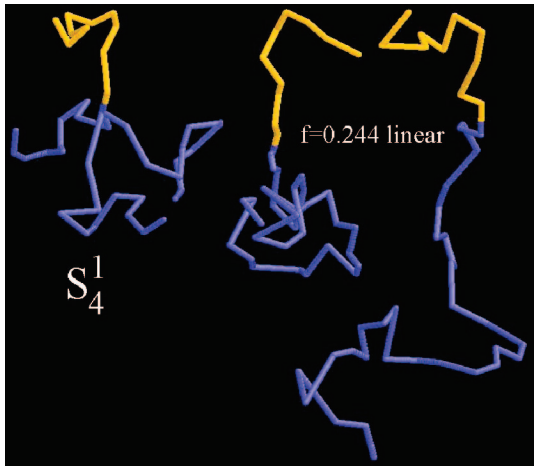

Figure 15. Snapshots of typical equilibrium conformations: S_4^1 star copolymer (left) vs linear copolymer in compact (middle) and spreaded form (right).

To examine the strong branching effect on the intramolecular level, let us concentrate on the comparison of S_4^1 star polymer with the equivalent composition $f = 0.244$ linear diblock molecule. The constraint imposed in S_4^1 is minimal; nonetheless, the phase changes from the Hex (observed for the linear diblock) to the FCC one for S_4^1. Some typical conformations for both architectures are depicted in Figure 15; these are stripped from the snapshots. First of all, we looked at the pitch of each phase; in-scale cross sections are shown side by side in Figure 16. The cross section of the FCC phase was made through the face of the elementary cell. The diameter of the spheres (for FCC) and that of the cylinders (for Hex) turned out to be very similar. That is to be expected as the yellow fragments (component B) in both architectures are the same (see Figure 15). However, the spacing of the hexagonal structure in both cases is very different (with the stars S_4^1 being packed much tighter) and the phase of S_4^1 being FCC and not Hex. We have the following explanation for this effect. Both architectures have the same density and the fraction of A and B beads. Given the cylinders

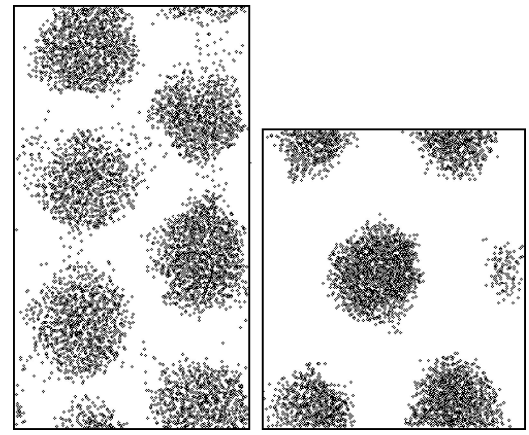

Figure 16. In-scale comparison of the FCC phase pitch in star diblock copolymer S_4^1 melt (left) vs that of the Hex phase in linear diblock copolymer melt with the same fraction $f = 0.244$ (right). Here B beads are represented via black dots.

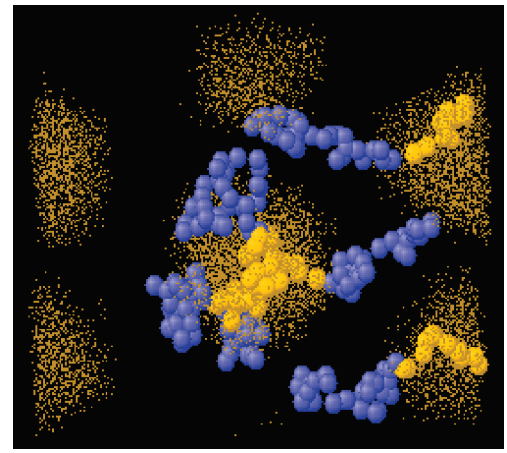

Figure 17. Typical molecular conformations of linear diblock molecules in Hex phase, $f = 0.244$. One should point out the existence of much spreaded coils of A component shown in blue.

of component B exist and have the same metrics in both cases, then the same hexagonal packing should also take place. This requires that the voids between the cylinders should be filled homogeneously by the beads of A component (see requirement 1 inning of this section).

Now, the question is narrowed to whether the homogeneous packing of these voids is possible in both architectures. In the case of linear diblock, the component A subchain is relatively long and has much conformational freedom (typical coiled and spreaded conformations are depicted in Figure 15). As is evident from the snapshot of $f = 0.244$ linear diblock melt (Figure 17), some of the blue subcoils are found well spread, indeed. On the contrary, in the case of S_4^1 molecule, one has three much shorter arms instead (Figure 15), and their spreading abilities are more limited (this is also mentioned above in the comment on scaling of R_g^A). This effect is confirmed by the snapshot of the S_4^1 melt (Figure 18). One can deduce that the voids between the cylinders cannot be filled homogeneously in a case of S_4^1 melt due to topological constraints imposed on the A subsystem. To establish the uniform density, the repulsion forces break cylinders into spheres and tight-pack these into the FCC phase instead. It is also worth noting that the difference between average R_g^A in both cases is only about 16% (see Tables 2 and 4), but the phase change takes place. A similar reason is found for the change of the phase from Hex to FCC in another case, S_6^5. Therefore, we can conclude that the internal branching is capable of inducing the phase change. This, in particular,

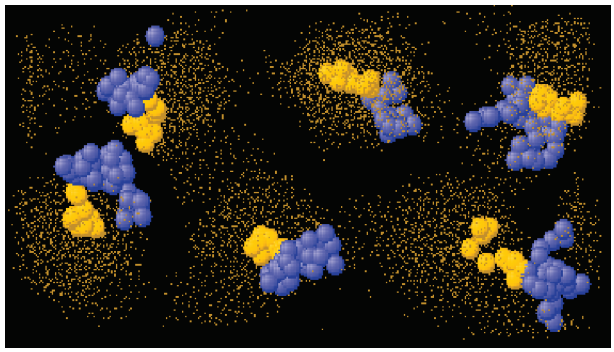

Figure 18. Typical molecular conformations of star diblock molecules S_4^1 in FCC phase, $f = 0.244$.

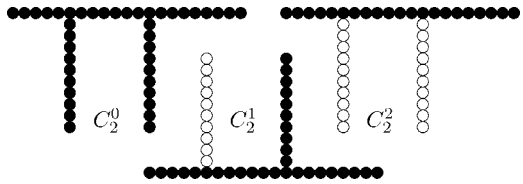

Figure 19. Combs with 2 side chains (A beads are shown in black, B beads in white).

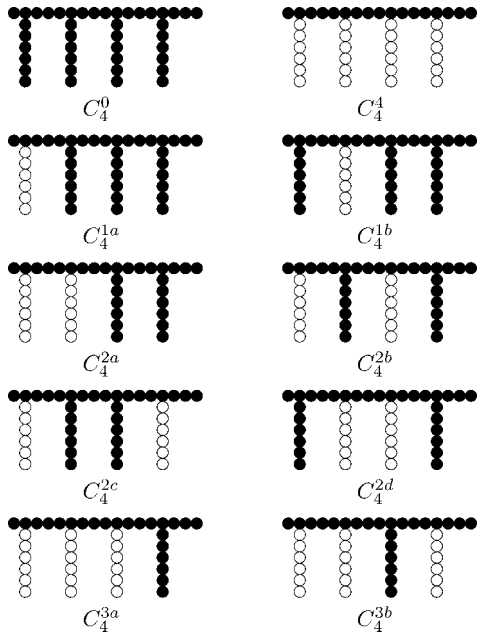

Figure 20. Combs with 4 side chains (A beads are shown in black, B beads in white).

happens when the constraints imposed on molecular conformations prevent the molecule to adopt the shape required for formation of some particular phase (as is observed in S_4^1 and S_6^5 cases).

6. Comb Diblocks

For the comb diblock copolymers we introduced the following notation. Architectures are denoted as C_p^q, where p is a number of side chains and q is a number of those made of beads B. The set of comb architectures examined in this study is presented in Figures 19 and 20. Similar properties have been studied as in the case of linear and star diblocks, which are collected in Tables 5 and 6.

In the case of comb diblock polymers we have observed both weak and strong branching effects, depending on the molecular

Table 5. Properties That Characterize Microphase Segregation in Comb Diblock Copolymer Melt at Different Values of B Component Fraction f^a

	f	R_{AB}	R_g	σ_1	σ_2	σ_3	T_{AB}	phase	ref
C_2^0	0.000		2.144	1.707	1.100	0.690		uni	uni
C_2^1	0.244	3.700	2.512	2.132	1.139	0.684	2.081	Hex	Hex
C_2^2	0.488	2.178	2.464	2.055	1.171	0.690	1.624	Lam	Lam
C_4^0	0.000		2.164	1.771	1.046	0.672		uni	uni
C_4^{1a}	0.146	3.426	2.276	1.879	1.088	0.682	1.794	BCC	BCC
C_4^{1b}	0.146	2.795	2.223	1.796	1.111	0.694	1.526	BCC	BCC
C_4^{2a}	0.293	3.023	2.316	1.946	1.059	0.673	1.909	**Lam**	**Hex**
C_4^{2b}	0.293	2.039	2.255	1.831	1.120	0.692	1.526	Hex	Hex
C_4^{2c}	0.293	1.941	2.328	1.930	1.106	0.684	1.496	Hex	Hex
C_4^{2d}	0.293	2.422	2.223	1.778	1.145	0.686	1.537	Hex	Hex
C_4^{3a}	0.439	2.003	2.212	1.786	1.108	0.689	1.602	**Lab**	**Lam**
C_4^{3b}	0.439	1.593	2.285	1.882	1.099	0.686	1.515	Lam	Lam
C_4^4	0.585	0.977	2.212	1.787	1.104	0.692	1.298	**Lab**	**Lam**

[a] The notations follow those in Table 1; the abbreviation "Lab" is used to denote the disordered labyrinth phase.

Table 6. Properties of A and B Subsystems in Comb Diblock Copolymer Melt at Different Values of B Component Fraction f^a

	f	R_g^A	R_g^B	σ_1^A	σ_1^B	T_A	T_B	phase	ref
C_2^0	0.000	2.144	0.000	1.707	0.000			uni	uni
C_2^1	0.244	2.078	1.245	1.752	1.093	1.347	0.874	Hex	Hex
C_2^2	0.488	1.727	2.566	1.482	2.385	0.925	1.283	Lam	Lam
C_4^0	0.000	2.164	0.000	1.771	0.000			uni	uni
C_4^{1a}	0.146	2.021	0.925	1.653	0.818	1.333	0.614	BCC	BCC
C_4^{1b}	0.146	2.104	0.907	1.766	0.801	1.172	0.622	BCC	BCC
C_4^{2a}	0.293	1.931	1.591	1.614	1.422	1.392	0.825	**Lam**	**Hex**
C_4^{2b}	0.293	1.916	2.278	1.610	2.162	1.131	1.164	Hex	Hex
C_4^{2c}	0.293	1.841	2.689	1.499	2.589	1.067	1.276	Hex	Hex
C_4^{2d}	0.293	2.016	1.621	1.733	1.456	1.058	0.859	Hex	Hex
C_4^{3a}	0.439	1.787	2.151	1.544	1.904	1.270	1.097	**Lab**	**Lam**
C_4^{3b}	0.439	1.693	2.572	1.413	2.321	1.048	1.442	Lam	Lam
C_4^4	0.585	1.516	2.504	1.316	2.101	0.818	1.370	**Lab**	**Lam**

[a] The notations follow those in Table 2.

architecture. Let us consider the cases which show the weak effect first. This is found in both C_2^1 and C_2^2 architectures with two chains and six architectures with four side chains, C_4^{1a}, C_4^{1b}, C_4^{2b}, C_4^{2c}, C_4^{2d}, and C_4^{3b}. The cases of C_2^1, C_2^2, C_4^{1a}, and C_4^{1b} can be seen as trivial; hence, we will concentrate on the C_4^{2b}, C_4^{2c}, and C_4^{2d}, all of which form hexagonal phase. Similarly to the case of linear diblock (Figure 12), we compared first the pitch of the phase in all three cases. The snapshots are shown in Figure 21 and appear to be quite the same. However, as one sees from Table 6, there is an essential difference between the radius of gyration of the B component, namely $R_g^B \sim 1.6$ for C_4^{2d} vs $R_g^B \sim 2.7$ for C_4^{2c}. The distributions of the R_g^B values provide more insight on this effect (see Figure 22). One can observe that in the case of C_4^{2b} and C_4^{2c} there are two maxima indicating two possible equilibrium conformations for the B beads to be arranged within the molecule. The internal connectivity of C_4^{2b} and C_4^{2c} molecules bears the similarity in the way that the B side chains are separated at least by one A side chain. As a result, in the relaxed conformation, the molecules adopt rather triblock form of BAB composition. This is illustrated in the snapshot (Figure 23), where some molecules are seen to interconnect two cylinders of the B phase. As follows from the distributions shown in Figure 22, this tendency is stronger for the C_4^{2c} architecture, where B chains are placed further apart. On the contrary, in C_4^{2a} and C_4^{2d} molecules, the B side chains are adjacent and the B side chains of the molecule are always closely packed together (single maximum in Figure 22, left). Hence, despite the fact that all three architectures, C_4^{2b}, C_4^{2c}, and C_4^{2d}, demonstrate quite the same Hex morphology, the arrangement of the molecules within the phase is rather different. The interconnection between the cylinders by an essential number of triblock-like molecules can influence, for instance, mechanical

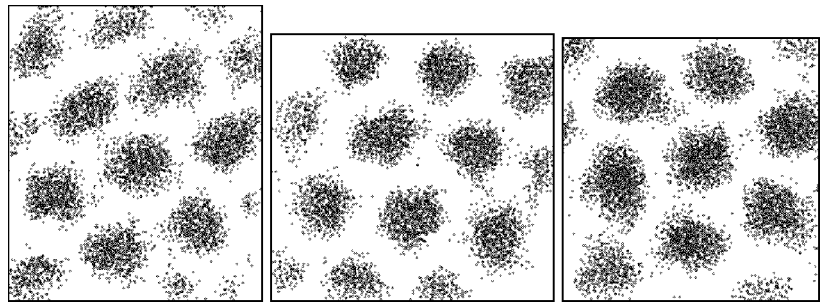

Figure 21. In-scale comparison of Hex phase pitch for the comb diblock copolymer melts of C_4^{2b} (left), C_4^{2c} (middle), and C_4^{2d} (right).

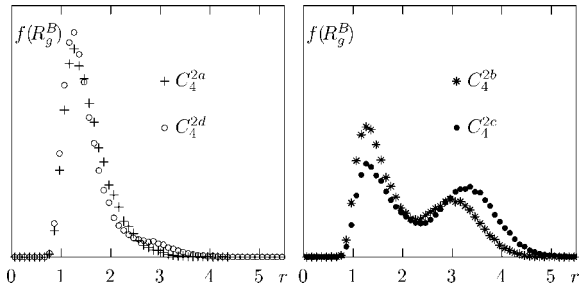

Figure 22. Distribution of partial radius of gyration R_g^B, single maximum in C_4^{2a} and C_4^{2d} melts (left) and double maxima form in C_4^{2b} and C_4^{2c} melts (right).

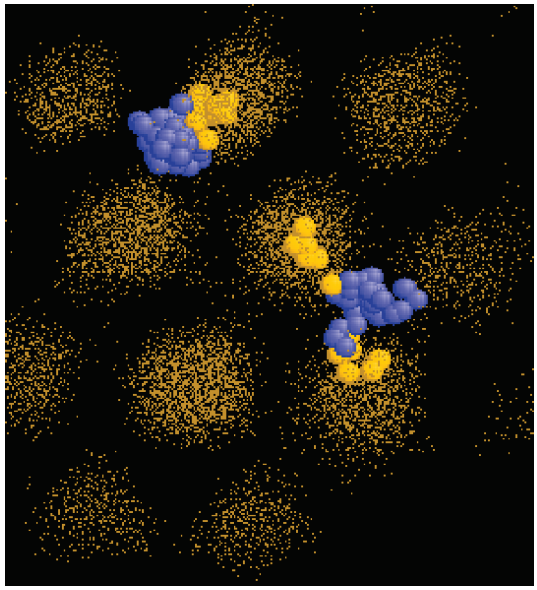

Figure 23. C_4^{2c} melt: normal coil molecular conformation (top left corner) and triblock-like BAB molecular conformation that leads to the interlink between the cylindrical structures (center right).

and other properties of the melt. This, however, is beyond the aim of current study.

A strong branching effect is observed in the cases of C_4^{3a}, C_4^{4}, and C_4^{2a} molecules. In the first two cases, the complicated structures are observed, which we will refer to as "labyrinth" (Lab) phase (see Figure 24) in place of the lamellar structure expected for the linear diblock with the same composition f. It is stable even after a very large number of $(8-10) \times 10^6$ DPD steps. It might be a bicontinuous phase, but this is not seen very clearly due to its irregular structure. The snapshot shown in Figure 25 suggests that the lamellar phase is not formed in this case due to insufficient length of the A parts of the molecules. The pitch of the expected lamellar phase is determined by the composition fraction f, whereas the A beads are mostly localized in the backbone and are too constrained to

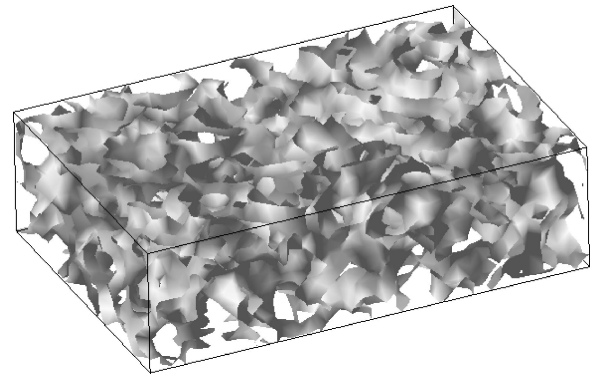

Figure 24. Density snapshot of labyrinth phase (Lab) obtained for the C_4^{3a} comb architecture.

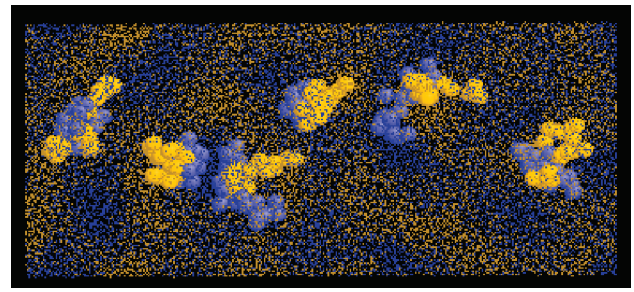

Figure 25. C_4^{3a} melt: strong conformational constraints on backbone beads A (shown in blue) are likely to be responsible for short-ranged disordered structure.

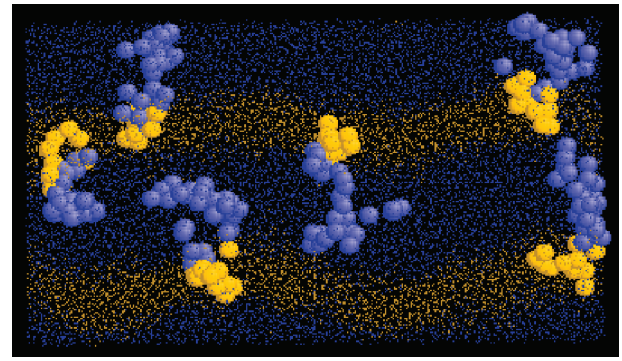

Figure 26. C_4^{2a} melt: enhancement of the lamellar structure by underlying symmetry in the arrangement of A beads (see Figure 19).

spread into the layer of required thickness. The backbone beads here act merely as a linkage for the side chains and cannot participate in the formation of the layers. As a result, short-range order structures are observed instead. It is interesting to note that a minor rearranging of side chains, as in C_4^{3b} architecture, is sufficient to bring a part of the backbone and

single A side chain into play and to form the lamellar phase.

Another interesting case is the C_4^{2a} architecture, for which the opposite shift of the phase occurs. Instead of the Hex phase observed for the linear diblock at the same composition *f*, the lamellar phase is found. It is quite evident that the effect is due to molecular symmetry of C_4^{2a}, which promotes the lamellar morphology (even more than in the case of linear diblock, see Figure 26).

7. Conclusions

We analyzed the peculiarities of the equilibrium morphologies observed for the star and comb diblock polymers with equal molecular mass but with the differences in both intramolecular architecture and composition fraction *f*. For each type of melt, its equilibrium morphology was compared with that of its linear diblock counterpart with the same value of *f*. In our DPD simulations we used the $NP_{XX}P_{YY}P_{ZZ}T$ ensemble, which is free from the problem of incommensurability between the box shape and the characteristic pitch of the phase. One of the outcomes is the restored evidence of the gyroid phase at $f \sim 0.34$, the issue of which was previously addressed.

In all cases, the final morphology can be seen as a compromise between three competing requirements: homogeneous space filling, minimal separation interface area, and preservation of molecular connectivity. Both cases of weak branching effect (the same phase is observed as for the linear diblock) and strong branching effect (the phase does change) are found.

The reason for a change to less ordered phase is the inconsistency between the required phase pitch and the connectivity constraints inside the molecule. For the linear diblock, each component has a connectivity of a single chain. In the case of star polymers, the arms of each component are grafted at the central bead, and this constraint does not allow them to spread out in the same way as a single chain and to fill in required space regions homogeneously. In the case of combs, the same effect is observed for the highly constrained backbone beads. As a result, the beads cannot be distributed homogeneously throughout the sample, and the phase observed for linear diblocks cannot be formed.

It is remarkable that in some cases the opposite effect is observed, e.g., promotion of more ordered lamellar phase (in place of a hexagonal one for the linear diblock) by suitable symmetry of the comb architecture.

Besides the macroscopical structural changes, we also observed a number of peculiarities in molecular conformations. Depending on the molecular architecture of comb polymer, different conformations and different molecular arrangements were observed in otherwise similar hexagonal phases. In several cases, the hexagonally arranged cylinders were found to be interlinked by comb molecules, which were found in rather triblock form of BAB form with the middle A part acting as a spacer. This is of great interest for considering mechanical properties of the polymer due to possible cross-linking effects of such conformations.

References and Notes

(1) Vogtle, F. *Supramolecular Chemistry: An Introduction*; John Wiley & Sons Ltd.: Chichester, 1993.
(2) Lehn, J. M. *Supramolecular Chemistry: Concepts and Perspectives*; Wiley-Interscience: Weinheim, 1995.
(3) Ariga, K.; Kunitake, T. *Supramolecular Chemistry—Fundamentals and Applications: Advanced Textbook*; Springer-Verlag: New York, 2006.
(4) Hadjichristidis, N.; Pispas, S.; Floudas, G. *Block Copolymers: Synthetic Strategies, Physical Properties, and Applications*; Wiley-Interscience: New York, 2002.
(5) Bates, F. S.; Frederickson, G. H. *Annu. Rev. Phys. Chem.* **1990**, *41*, 525–557.
(6) Corberi, F.; Gonnella, G.; Lamura, A. *Phys. Rev. Lett.* **1999**, *83*, 4057–4060.
(7) *Block Copolymers in Nanoscience*; Lazzari, M., Liu, G., Lecommandoux, S., Eds.; Wiley: New York, 2006.
(8) Krusin-Elbaum, L.; Guarini, K.; Black, C. T.; Tuominen, M. T.; Russell, T. P. *Science* **2000**, *290*, 2126–2129.
(9) Hamley, I. W. *Nanotechnology* **2003**, *14*, R39–R54.
(10) Olvera de la Cruz, M.; Sanchez, I. C. *Macromolecules* **1986**, *19*, 2501–2508.
(11) Vavasour, J. D.; Whitmore, M. D. *Macromolecules* **1992**, *25*, 5477–5486.
(12) Shinozaki, A.; Jasnow, D.; Balazs, A. C. *Macromolecules* **1994**, *27*, 2496–2502.
(13) Matsen, M. W.; Bates, F. S. *Macromolecules* **1996**, *29*, 1091–1098.
(14) Matsen, M. W. *J. Phys.: Condens. Matter* **2002**, *14*, R21–R47.
(15) Cochran, E. W.; Garcia-Cervera, C. J.; Fredrickson, G. H. *Macromolecules* **2006**, *39*, 2449–2451.
(16) Hamley, I. W.; Fairclough, J. P. A.; Ryan, A. J.; Maic, S. M.; Booth, C. *Phys. Chem. Chem. Phys.* **1999**, *1*, 2097–2101.
(17) Castelletto, V.; Hamley, I. W. *Curr. Opin. Solid State Mater. Sci.* **2004**, *8*, 426–438.
(18) Lu, Z.; Liu, G.; Duncan, S. *Macromolecules* **2004**, *37*, 174–180.
(19) Weyersberg, A.; Vilgis, T. A. *Phys. Rev. E* **1993**, *48*, 377–391.
(20) Hamley, I. W. *Macromol. Theory Simul.* **2000**, *9*, 363–380.
(21) Schultz, A. J.; Hall, C. K.; Genzer, J. *J. Chem. Phys.* **2002**, *117*, 10329–10338.
(22) Martínez-Veracoechea, F. J.; Escobedo, F. *A J. Chem. Phys.* **2006**, *125*, 104907.
(23) Matsen, M. W.; Griffiths, G. H.; Wickham, R. A.; Vassiliev, O. N. *J. Chem. Phys.* **2006**, *124*, 024904.
(24) Martinez-Veracoechea, F. J.; Escobedo, F. A. *Macromolecules* **2007**, *40*, 7354–7365.
(25) Soto-Figueroa, C.; Rodríguez-Hidalgo, M. R.; Martínez-Magadán, J. M. *Polymer* **2005**, *46*, 7485–7493.
(26) Frenkel, D.; Smit, B. *Understanding Molecular Simulation: From Algorithms to Applications*; Academic: San Diego, 1996.
(27) Groot, R. D.; Madden, T. G. *J. Chem. Phys.* **1998**, *108*, 8713–8724.
(28) Turner, C. M.; Sheller, N. B.; Foster, M. D.; Lee, B.; Corona-Galvan, S.; Quirk, R. P.; Annis, B.; Lin, J. S. *Macromolecules* **1998**, *31*, 4372–4375.
(29) Xu, Y.; Liu, F. H.; Hu, Y. *Mol. Simul.* **2006**, *32*, 375–383.
(30) Huang, C. I.; Chen, C. M. *ChemPhysChem* **2007**, *8*, 2588–2594.
(31) Huang, C. I.; Lin, Y. C. *Macromol. Rapid Commun.* **2007**, *28*, 1634–1639.
(32) Zhong, C.; Liu, D. *Macromol. Theory Simul.* **2007**, *16*, 141–157.
(33) Huang, C. I.; Yu, H. T. *Polymer* **2007**, *48*, 4537–4546.
(34) Soto-Figueroa, C.; Vicente, L.; Martínez-Magadán, J. M.; Rodríguez-Hidalgo, M. R. *J. Phys. Chem. B* **2007**, *111*, 11756–11764.
(35) Groot, R. D.; Warren, P. B. *J. Chem. Phys.* **1997**, *107*, 4423–4435.
(36) Español, P.; Warren, P. *Europhys. Lett.* **1995**, *30*, 191–196.
(37) Nikunen, P.; Karttunen, M.; Vattulainen, I. *Comput. Phys. Commun.* **2003**, *153*, 407–423.
(38) Wilson, M. R. In *Structure and Bonding*; Mingos, M., Ed.; Springer-Verlag: Heidelberg, 1999; Vol. *94*, pp 42−64.
(39) Liu, W.; Qian, H. J.; Lu, Z. Y.; Li, Z. S.; Sun, C. C. *Phys. Rev. E* **2006**, *74*, 021802.
(40) Ilnytskyi, J. M.; Neher, D. *J. Chem. Phys.* **2007**, *126*, 174905.
(41) Hoover, W. G. *Phys. Rev. A* **1985**, *31*, 1695–1697.
(42) Wijmans, C. M.; Smit, B.; Groot, R. D. *J. Chem. Phys.* **2001**, *114*, 7644–7654.
(43) Padding, J. T.; Briels, W. J. *J. Chem. Phys.* **2001**, *115*, 2846–2859.
(44) Parrinello, M.; Rahman, A. *J. Appl. Phys.* **1981**, *52*, 7182–7190.
(45) Jakobsen, A. F. *J. Chem. Phys.* **2005**, *122*, 124901.
(46) Ilnytskyi, J. M.; Holovatch, Yu. *Condens. Matter Phys.* **2007**, *10*, 539–551.
(47) Nikunen, P.; Vattulainen, I.; Karttunen, M. *Phys. Rev. E* **2007**, *75*, 036713.
(48) Soto-Figueroa, C.; Rodríguez-Hidalgo, M. R.; Martínez-Magadán, J. M.; Vicente, L. *Macromolecules* **2008**, *41*, 3297–3304.
(49) Xu, Y.; Feng, J.; Liu, H.; Hu, Y. *Mol. Simul.* **2008**, *34*, 559–565.
(50) Spenley, N. A. *Europhys. Lett.* **2000**, *49*, 534–540.

MA801045Z